Valence Orbitals Driving the Spin Dynamics in a Rare-Earth Single-Atom Magnet

A. Curcella, D. Sblendorio, S. Rusponi, M. Pivetta, F. Patthey, and H. Brune*

Institute of Physics, Ecole Polytechnique Fédérale de Lausanne, CH-1015 Lausanne, Switzerland

We combine spin-polarized scanning tunneling microscopy with quantum master equation analysis to investigate the spin dynamics of the single atom magnet Dy on graphene/Ir(111). By performing reading and writing experiments, we show that the strongly spin polarized $5d6s$ valence shells, as well as their intra-atomic exchange coupling to the $4f$ shell, determine the pathways for magnetization relaxation and thus the spin dynamics. The good quantum number that determines which states are stable and which mechanisms for reversal exist in a given crystal field is the atomic total angular momentum J_z^{tot} and not the commonly considered J_z^{4f} of the $4f$ shell only.

Because of their strongly localized and therefore well-protected $4f$ electrons, rare-earth atoms enabled the realization of single-ion molecular magnets (SIMs) [1–4] and single-atom magnets (SAMs) [5–12]. A fundamental understanding of their spin dynamics is mandatory in the operation of single rare-earth atoms as qubits and memories [13–28].

The occupation of the $4f$ orbitals is well described by Hund's rules, resulting in atomiclike spin and orbital momenta that are strongly coupled. A spin polarization of the valence shells ($5d$ and $6s$) is also frequently expected, however, yielding only a small extra contribution to the total momentum. Consequently, the rare earth atoms' magnetic properties are described exclusively in terms of the total angular momentum of the $4f$ shell, $|J^{4f}\rangle$. Hence, spin dynamics in SAMs and SIMs is explained as transitions between states defined by the $|J^{4f}\rangle$ projection onto the quantization axis $|J_z^{4f}\rangle$ ($4f$ model) [2–6,10,11].

While this approach applies to those cases where the lanthanide atoms are in a $+3$ oxidation state, as in most SIMs, recent theoretical works suggest that this description is not always valid [29,30] and that the valence electrons can play an essential role. For instance, they mediate ferromagnetic exchange coupling in dilanthanide complexes [31,32]. In view of the strong valence-$4f$ intra-atomic exchange coupling, the magnetic state of a rare-earth atom should then be described in terms of the total angular momentum $|J^{\text{tot}}\rangle = |J^{4f}\rangle \otimes |S^{5d}\rangle \otimes |S^{6s}\rangle$, where the total angular momentum of the $5d$ and $6s$ shells is approximated by the spin momentum only, since the

orbital momentum of these shells is either zero ($6s$), or strongly quenched by hybridization with the surrounding atoms ($5d$). This scenario implies a paradigm shift and was labeled FV-magnetism [29,30]. If it holds, the spin dynamics is determined by the transition probabilities between the projections of $|J^{\text{tot}}\rangle$ onto the quantization axis, $|J_z^{\text{tot}}\rangle$ ($4f5d6s$ model).

The most important difference between these descriptions is that the associated Hilbert spaces have different channels for quantum tunneling of the magnetization (QTM). In the traditional $4f$ model, and for an atom in a crystal field (CF) with k-fold symmetry, QTM involves states differing by $\Delta J_z^{4f} = kn$, with $n \in \mathbb{Z}$. In the $4f5d6s$ model, QTM takes place via states with $\Delta J_z^{\text{tot}} = kn$.

Here we present direct experimental evidence that the spin dynamics of a rare-earth SAM is determined by FV-magnetism. We use spin-polarized scanning tunneling microscopy (SP-STM) to investigate the magnetization switching rates of individual Dy atoms on graphene on Ir(111) [6] as a function of temperature and tunnel voltage. We find evidence for two low-lying channels for QTM that only exist in the $4f5d6s$ model. Within this model, all switching rates are reproduced by quantum master equations. In contrast, the conventional $4f$ model, which exhibits only one low-energy channel for QTM, fails to describe the experimental results.

We choose Dy/gr/Ir(111), as previous knowledge of this system determines the Hamiltonians predicting the magnetic level schemes for both models, thus enabling the most realistic comparison between the two. X-ray absorption spectroscopy (XAS) and x-ray magnetic circular dichroism (XMCD) reveal a $4f^{10}$ filling with $|J^{4f} = 8\rangle$ and a $|J_z^{4f} = \pm 7\rangle$ ground state with out-of-plane easy magnetization axis. The XMCD magnetization curves exhibit two steps due to level crossings that determine the energy separation of the low-lying doublets [6]. STM reports
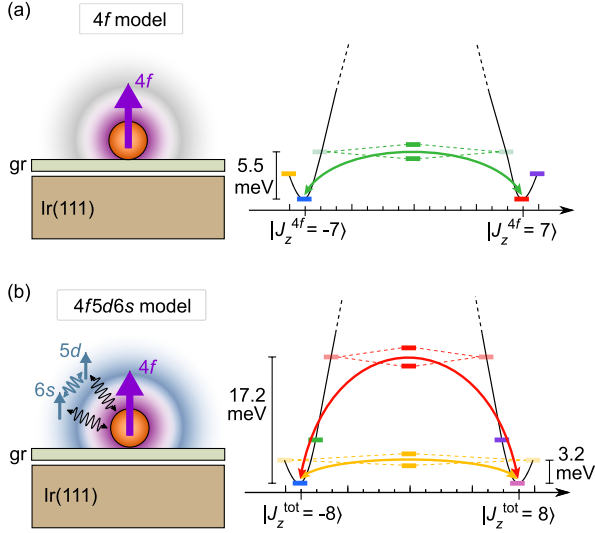
FIG. 1. Sketches (left) and magnetic level schemes (right) of (a) the $4f$ and (b) the $4f5d6s$ model, as determined from published XMCD data. In (a) there is only one QTM path available, via $|J_z^{4f} = \pm 6\rangle$ (green arrow) while in (b) two such paths exist, via $|J_z^{\text{tot}} = \pm 9\rangle$ (yellow) and $|J_z^{\text{tot}} = \pm 6\rangle$ (red). States with the same color are mixed by the sixfold crystal field.

exclusive adsorption in the sixfold graphene hollow site, determining the CF symmetry [6], and SP-STM reveals a large spin polarization of the $5d6s$ shells [33] that is rationalized by the transfer of 0.74 ± 0.03 electrons to the substrate [34]. This valence spin is exchange coupled by almost 100 meV to the spin of the $4f$ shell, and density functional theory (DFT) calculations show that this exchange originates from both, $5d$ and $6s$ shells [33].

The magnetic quantum level schemes accounting for these findings are presented in Fig. 1. The orbital resolved composition, energies, and the splittings of the doublets are given in Table I. The slightly different energies of the excited states in the two models are required to reproduce the steps in the XMCD magnetization curve due to

TABLE I. Out-of-plane projected eigenstates $|J_z^{4f}\rangle$ ($4f$ model) and $|J_z^{\text{tot}}\rangle$ ($4f5d6s$ model), their orbital resolved composition in $\hbar$ units, eigenvalues E, and energy splitting $\hbar\omega$ of the doublets.

	J_z^{4f}	S_z^{5d}	S_z^{6s}	E (meV)	$\hbar\omega$ (μeV)
$\lvert J_z^{4f}\rangle$					
$\lvert \pm 7\rangle$	± 7.0	$\cdots$	$\cdots$	0	0
$\lvert \pm 8\rangle$	± 8.0	$\cdots$	$\cdots$	3.0	0
$\lvert \pm 6\rangle$	0	$\cdots$	$\cdots$	5.5	13
$\lvert J_z^{\text{tot}}\rangle$					
$\lvert \pm 8\rangle$	± 7.1	± 0.5	± 0.5	0	0
$\lvert \pm 9\rangle$	0	0	0	3.2	0.0036
$\lvert \pm 7\rangle$	± 6.3	± 0.4	± 0.4	5.8	0
$\lvert \pm 6\rangle$	0	0	0	17.2	13

the different Zeeman splittings. In the $4f$ model, the $|J_z^{4f} = \pm 7\rangle$ ground state doublet is protected from QTM and spin reversal takes place via excitation to the split doublet originating from the mixed $|J_z^{4f} = \pm 6\rangle$ states. For the $4f5d6d$ model, an exact evaluation of the spin polarization of the $5d$ and $6s$ shells from DFT is difficult due to the large spatial extent of these orbitals and their hybridization with C $2p$ states; thus, we assume for simplicity a half-integer spin for each valence shell, $S^{5d} = \frac{1}{2}$ and $S^{6s} = \frac{1}{2}$. Now we get a $|J_z^{\text{tot}} = \pm 8\rangle$ ground state doublet that is again protected from QTM, however, there exist two pathways for magnetization reversal, namely, via the $|J_z^{\text{tot}} = \pm 9\rangle$ and the $|J_z^{\text{tot}} = \pm 6\rangle$ split doublets.

Constant-height tunnel current traces recorded with the STM tip centered on top of isolated Dy adatoms show a two-state telegraph signal due to the magnetization reversal of Dy, see Fig. 2(a). The high conductance (HC) and low conductance (LC) states correspond to parallel and
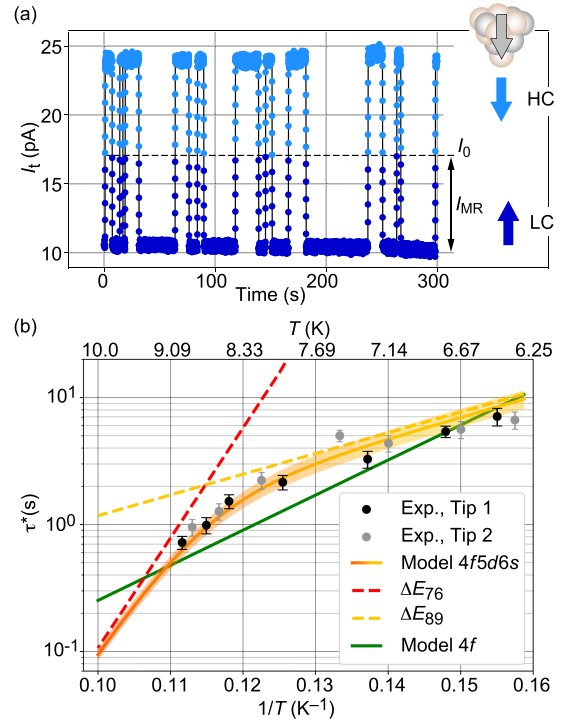

FIG. 2. (a) Telegraph signal of Dy ($T = 6.3$ K, bias voltage $V_b = 1$ mV, set current $I_t = 10$ pA in the LC state). I_0 is the nonpolarized and I_{MR} the magnetoresistive current. Right: alignment of tip spin polarization at E_F and Dy momentum in both states. (b) Arrhenius plot of the spin lifetime. Experiment: black and grey dots ($V_b = 1$ mV, set current $I_t = 10$ pA in the LC state). $4f5d6s$ model: red-to-yellow curve, the shaded area shows the accuracy of the fit with $B_{\text{tip}} = -60 \pm 5$ mT. Yellow and red dashed lines show τ^* with QTM exclusively via $|J_z^{\text{tot}} = \pm 9\rangle$ or $|J_z^{\text{tot}} = \pm 6\rangle$, corresponding to activation energies $\Delta E_{89} = E(|J_z^{\text{tot}} = 9\rangle) - E(|J_z^{\text{tot}} = 8\rangle)$ and $\Delta E_{76} = E(|J_z^{\text{tot}} = 6\rangle) - E(|J_z^{\text{tot}} = 7\rangle)$, respectively. $4f$ model: green curve. $\rho_T = -0.8$ for both models.

TABLE II.   Hamiltonian terms in the two models.

	4f model		4f5d6s model
J	$J^{4f} = 8$		$J^{\text{tot}} = 9$ $(J^{4f} = 8, S^{5d} = ½, S^{6s} = ½)$
$\hat{H}_{\text{ex}}$	$\cdots$		$(g_J - 1)[\mathcal{J}_{4f-6s}(\hat{J}^{4f} \cdot \hat{S}^{6s}) + \mathcal{J}_{4f-5d}(\hat{J}^{4f} \cdot \hat{S}^{5d})] + \mathcal{J}_{5d-6s}(\hat{S}^{5d} \cdot \hat{S}^{6s})$
$\hat{H}_{\text{CF}}$	$B_2^0\hat{O}_2^0 + B_4^0\hat{O}_4^0 + B_6^0\hat{O}_6^0 + B_6^6\hat{O}_6^6$		$B_2^0\hat{O}_2^0 + B_4^0\hat{O}_4^0 + B_6^0\hat{O}_6^0 + B_6^6\hat{O}_6^6$
$\hat{H}_Z$	$\mu_B g_J J_z^{4f} B_{\text{tip}}$		$\mu_B(g_J J_z^{4f} + g S_z^{sd}) B_{\text{tip}}$
$\hat{H}_{\text{sp-ph}}$	$(\hat{J}_-^{4f})^2 + (\hat{J}_+^{4f})^2 + \{\hat{J}_-^{4f}, \hat{J}_z^{4f}\} + \{\hat{J}_+^{4f}, \hat{J}_z^{4f}\}$		$(\hat{J}_-^{4f})^2 + (\hat{J}_+^{4f})^2 + \{\hat{J}_-^{4f}, \hat{J}_z^{4f}\} + \{\hat{J}_+^{4f}, \hat{J}_z^{4f}\}$
$\hat{H}_{\text{sp-el}}$	$\hat{\sigma} \cdot \hat{J}^{4f}$		$\hat{\sigma} \cdot \hat{S}^{sd}$

antiparallel alignment of the tip and Dy spin polarizations. Note the large spin contrast, expressed by the large fraction of the magnetoresistive to the nonpolarized current, I_{MR} and I_0, respectively. The individual lifetimes of both states, τ_{HC} and τ_{LC}, are determined by fitting histograms of residence times. To describe the spin dynamics, it suffices to consider a single characteristic lifetime, $\tau^* = \tau_{\text{HC}}\tau_{\text{LC}}/(\tau_{\text{HC}} + \tau_{\text{LC}})$ [35]. The occupancies of the individual states are given by τ^*/τ_{HC} and τ^*/τ_{LC}.

Figure 2(b) shows the Arrhenius plot of the spin lifetime τ^* under reading conditions, i.e., with a tunnel voltage below any of the excitation energies of the magnetic quantum levels. The spin lifetime decreases with increasing temperature, evidencing thermally assisted magnetization reversal. The data show a transition between a shallow slope at low T and a much steeper one at high T, with the change occurring around 8.3 K. This observation indicates the presence of two reversal paths with different activation energies.

To distinguish quantitatively between both models, the spin dynamics is calculated via a master equation describing the transition probabilities between the eigenstates of the system in the presence of phonon and electron scattering [14,17,21,64,65]. The Hamiltonian can be written as

$$\hat{H} = \hat{H}_{\text{ex}} + \hat{H}_{\text{CF}} + \hat{H}_Z + \hat{H}_{\text{sp-ph}} + \hat{H}_{\text{sp-el}} \qquad (1)$$

with the respective expressions used for these terms in both models listed in Table II and detailed in [35]. The first three terms define the Dy eigenstates displayed in Fig. 1, while $\hat{H}_{\text{sp-ph}}$ and $\hat{H}_{\text{sp-el}}$ describe the Dy spin scattering with phonons and electrons, respectively.

Only a limited number of free parameters is available to reproduce the data, namely, the tip stray field B_{tip} and spin polarization ρ_T, the ratio ζ between inelastic and elastic tunneling, the surface to adatom hopping probability ς_S, and the spin-phonon scattering efficiency ν_{ph} [35]. Two additional fit parameters are the energy E and splitting $\hbar\omega$ of $|J_z^{\text{tot}} = \pm 6\rangle$, while for the remaining eigenstates these quantities are determined from previous XAS and XMCD experiments.

The observed change in slope in Fig. 2(b) is very well reproduced by the 4f5d6s model (red-to-yellow curve),

while the 4f model (green line) completely fails. In both models, the thermally activated spin dynamics is largely dominated by scattering with substrate electrons, while spin-lattice relaxation is almost negligible in the entire temperature range [35]. This is expected since the high stiffness of graphene implies a low phonon density in the low energy range of interest.

In the 4f5d6s model and at low temperatures, scattering with substrate electrons induces spin transitions $(\Delta J_z^{\text{tot}} = \pm 1)$ driving the Dy spin from the ground doublet $|J_z^{\text{tot}} = \pm 8\rangle$ to the first excited one $|J_z^{\text{tot}} = \pm 9\rangle$, from where the magnetization reverses via QTM. As we increase the temperature, higher energy states become populated, including the high energy split doublet $|J_z^{\text{tot}} = \pm 6\rangle$. Despite being much less populated than $|J_z^{\text{tot}} = \pm 9\rangle$, the larger energy splitting of $|J_z^{\text{tot}} = \pm 6\rangle$ results in a more efficient QTM. The reversal via $|J_z^{\text{tot}} = \pm 6\rangle$ starts to be activated at about 8.3 K, has a nearly equal weight as reversal via $|J_z^{\text{tot}} = \pm 9\rangle$ at roughly 9 K, and largely dominates for $T \geq 10$ K.

The 4f model has a single thermal-assisted QTM channel between $|J_z^{4f} = \pm 6\rangle$ resulting in a straight line in the Arrhenius of τ^*. This line is too steep at low T and too shallow at high T compared to the data.

The strength of the 4f5d6s model is further confirmed by experiments under writing conditions, where the magnetic quantum states of Dy are manipulated by electrons tunneling from or to the tip. Figures 3(a)–3(c) show the spin lifetime, HC occupancy, and magnetoresistance as a function of bias voltage V_b at $T = 6.7$ K. The experimental data show small variations in τ^* and an almost flat HC occupancy at 50% for $|V_b| \leq 5$ mV, while τ^* is strongly reduced and strong spin-torque effects are observed at higher biases. The experimental behavior is again very well reproduced by the 4f5d6s model, while the 4f model is clearly unsatisfactory [66]. The ratio of the magnetoresistive to the nonpolarized current in Fig. 3(c) is only matched by the 4f5d6s model. Matching it in the 4f model results in too short relaxation times compared to the experimental τ^* in Fig. 3(a).

The bias dependence of the HC occupancy illustrates the difference between the two models very well. The measured staircase behavior can only be reproduced by a multipath
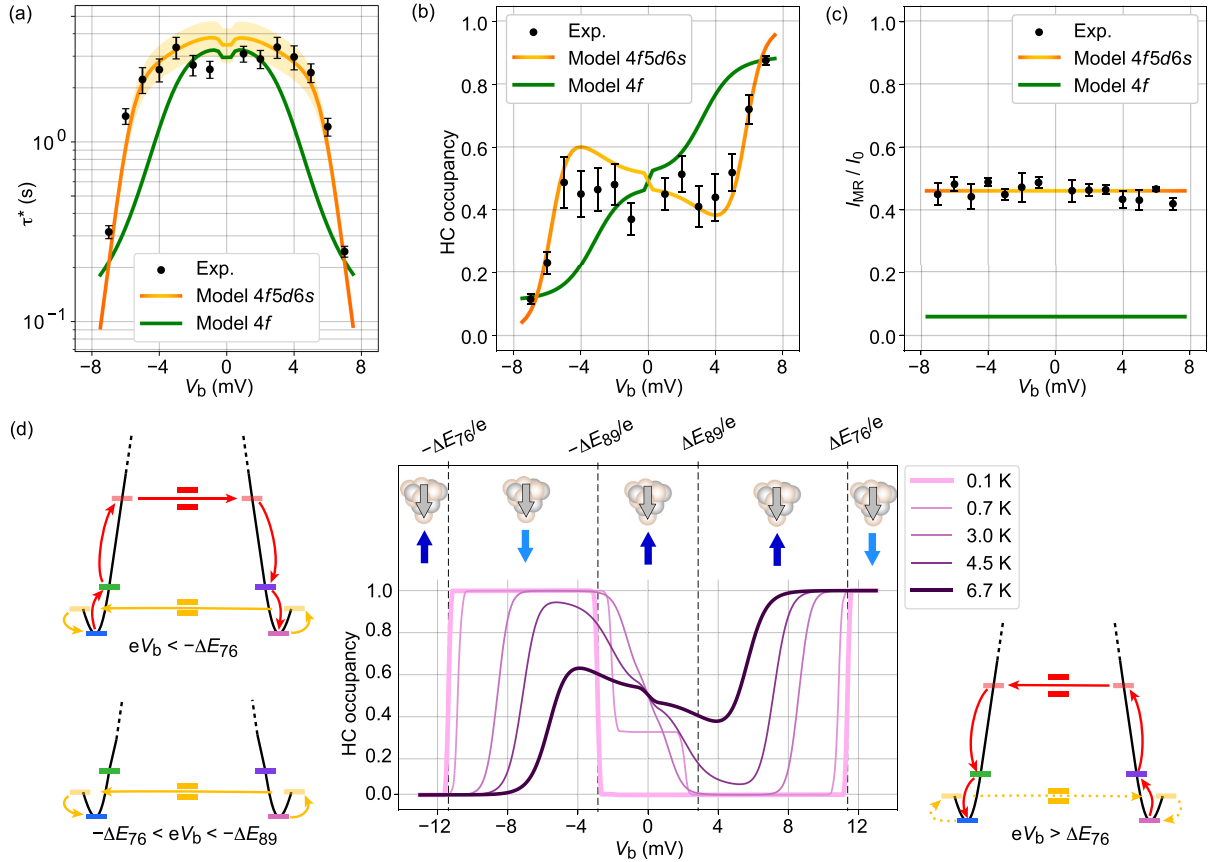
FIG. 3. (a) Spin lifetimes, (b) HC occupancy, and (c) ratio of magnetoresistive to nonpolarized tunneling current vs V_b (black dots, $T = 6.7$ K, set current $I_t = 10$ pA in the LC state). Lines show calculations with the $4f5d6s$ model (red to orange shaded according to QTM via $|J_z^{\text{tot}} = \pm 9\rangle$ or $|J_z^{\text{tot}} = \pm 6\rangle$) and the $4f$ model (green line) ($B_{\text{tip}} = -45$ mT, $\rho_T = -0.8$). The shaded area shows the accuracy of the fit with variations of B_{tip} within ± 5 mT. (d) HC occupancy vs bias predicted by the $4f5d6s$ model for a fully spin-down polarized tip ($B_{\text{tip}} = -45$ mT, $\rho_T = -1.0$); top: alignment of tip spin polarization and Dy momentum vs bias. Sketches on the left (right) show the spin reversal pathways for the indicated negative (positive) bias ranges.

reversal model, while a monotonic dependence is predicted by a single-path reversal model. Calculations reported in Fig. 3(d) show that the observed dependence results from steps, appearing at characteristic biases, progressively smoothed with increasing temperature. The origin of these steps is elucidated by looking at the extreme case of 0.1 K and for a fully spin-down polarized tip ($\rho_T = -1.0$) shown as a thick pink line. For $e|V_b| < 3.2$ meV $= \Delta E_{89} = E(|J_z^{\text{tot}} = 9\rangle) - E(|J_z^{\text{tot}} = 8\rangle)$, only the ground state favored by the tip stray field $|J_z^{\text{tot}} = 8\rangle$, with the Dy momentum pointing up, is occupied. Increasing $|V_b|$ opens up inelastic scattering to the next lying eigenstates, progressively activating magnetization reversal pathways. Reaching the first threshold on the negative bias side, where the fully spin-down polarized tip induces $\Delta J_z^{\text{tot}} = +1$ transitions, Dy is pumped to $|J_z^{\text{tot}} = 9\rangle$, from where the Dy spin tunnels through the barrier to $|J_z^{\text{tot}} = -9\rangle$ before relaxing to $|J_z^{\text{tot}} = -8\rangle$, see sketch on the lower left in Fig. 3(d). As a result, the Dy spin state switches from $|J_z^{\text{tot}} = 8\rangle$ to $|J_z^{\text{tot}} = -8\rangle$, corresponding to a HC occupancy of 1 (spin pumping). Backward paths are forbidden since (i) the

tunneling current only generates spin-increasing transitions, thus preventing the way back via $|J_z^{\text{tot}} = -8\rangle$ to $|J_z^{\text{tot}} = -9\rangle$; (ii) at this bias, the electron energy is not sufficient to promote transitions from $|J_z^{\text{tot}} = -8\rangle$ to $|J_z^{\text{tot}} = -7\rangle$ and farther to the top of the barrier; (iii) spin scattering with phonons and surface conduction electrons has negligible effect at this temperature. Therefore the Dy atom stays frozen in the $|J_z^{\text{tot}} = -8\rangle$ state until $eV_b \leq -\Delta E_{76} = -11.4$ meV, where tunneling electrons can promote transitions from there to $|J_z^{\text{tot}} = -7\rangle$ and successively to $|J_z^{\text{tot}} = -6\rangle$. QTM then induces transitions to $|J_z^{\text{tot}} = 6\rangle$, from where the spin can relax to $|J_z^{\text{tot}} = 8\rangle$. Note that under these bias conditions, the Dy spin cyclically reverses, see sketch on the upper left in Fig. 3(d). However, the probability of finding it in $|J_z^{\text{tot}} = 8\rangle$ is dominant. Writing is obtained by simply stopping the injection of the tunneling current in the desired HC or LC state, as identified via I_{MR}.

At positive bias, electrons of the considered tip drive $\Delta J_z^{\text{tot}} = -1$ transitions, and consequently they generate transitions from $|J_z^{\text{tot}} = 8\rangle$ to $|J_z^{\text{tot}} = 7\rangle$, without changing the HC occupancy. Upon reaching the threshold

$eV_b = \Delta E_{76}$, the Dy gets pumped into $|J_z^{\text{tot}} = 6\rangle$. The spin can then tunnel to $|J_z^{\text{tot}} = -6\rangle$, where it relaxes to $|J_z^{\text{tot}} = -8\rangle$. Again, under the effect of a continuous tunneling current, the spin will cyclically switch back to $|J_z^{\text{tot}} = 8\rangle$, via the yellow dotted path shown in the right sketch of Fig. 3(d). However, the probability of finding it in $|J_z^{\text{tot}} = -8\rangle$ is largely dominant.

We have demonstrated that the spin dynamics of Dy atoms on graphene on Ir(111) is governed by FV-magnetism, determining the Hilbert space and the QTM channels available for magnetization reversal. The same is expected to apply to other isolated spins whenever several electronic shells are spin polarized. This goes beyond lanthanides, from $3d$ elements [28,67] to actinides [68], underlining the general implications of our Letter. The role of the polarized valence shells is reminiscent of the one played by delocalized radicals in SIMs where a lanthanide center is exchange coupled with a delocalized radical ligand [69–74], or in dilanthanide radical-bridged complexes [71,75,76]. The radical modifies the spin reversal path and consequently can be used to improve the magnetic stability of the single molecule magnets. However, the strength of this exchange only amounts to a few meV, limiting its effect to temperatures lower than about 30 K [71,76], while the larger FV coupling is expected to determine the spin dynamics up to higher temperatures.

---

[*] harald.brune@epfl.ch

[1] N. Ishikawa, M. Sugita, T. Ishikawa, S. Koshihara, and Y. Kaizu, Lanthanide double-decker complexes functioning as magnets at the single-molecular level, J. Am. Chem. Soc. **125**, 8694 (2003).

[2] K. S. Pedersen, A.-M. Ariciu, S. McAdams, H. Weihe, J. Bendix, F. Tuna, and S. Piligkos, Toward molecular 4f single-ion magnet qubits, J. Am. Chem. Soc. **138**, 5801 (2016).

[3] C. A. P. Goodwin, F. Ortu, D. Reta, N. F. Chilton, and D. P. Mills, Molecular magnetic hysteresis at 60 kelvin in dysprosocenium, Nature (London) **548**, 439442 (2017).

[4] F.-S. Guo, B. M. Day, Y.-C. Chen, M.-L. Tong, A. Mansikkamki, and R. A. Layfield, Magnetic hysteresis up to 80 kelvin in a dysprosium metallocene single-molecule magnet, Science **362**, 1400 (2018).

[5] F. Donati, S. Rusponi, S. Stepanow, C. Wäckerlin, A. Singha, L. Persichetti, R. Baltic, K. Diller, F. Patthey, E. Fernandes, J. Dreiser, Ž. Šljivančanin, K. Kummer, C. Nistor, P. Gambardella, and H. Brune, Magnetic remanence in single atoms, Science **352**, 318 (2016).

[6] R. Baltic, M. Pivetta, F. Donati, C. Wäckerlin, A. Singha, J. Dreiser, S. Rusponi, and H. Brune, Superlattice of single atom magnets on graphene, Nano Lett. **16**, 7610 (2016).

[7] F. D. Natterer, K. Yang, W. Paul, P. Willke, T. Choi, T. Greber, A. Heinrich, and C. Lutz, Reading and writing single-atom magnets, Nature (London) **543**, 226 (2017).

[8] F. D. Natterer, F. Donati, F. Patthey, and H. Brune, Thermal and Magnetic-Field Stability of Holmium Single-Atom Magnets, Phys. Rev. Lett. **121**, 027201 (2018).

[9] F. Donati, S. Rusponi, S. Stepanow, L. Persichetti, A. Singha, D. M. Juraschek, C. Wäckerlin, R. Baltic, M. Pivetta, K. Diller, C. Nistor, J. Dreiser, K. Kummer, E. Velez-Fort, N. A. Spaldin, H. Brune, and P. Gambardella, Unconventional Spin Relaxation Involving Localized Vibrational Modes in Ho Single-Atom Magnets, Phys. Rev. Lett. **124**, 077204 (2020).

[10] F. Donati, M. Pivetta, C. Wolf, A. Singha, C. Wäckerlin, R. Baltic, E. Fernandes, J.-G. de Groot, S. Lamia Ahmed, L. Persichetti, C. Nistor, J. Dreiser, A. Barla, P. Gambardella, H. Brune, and S. Rusponi, Correlation between electronic configuration and magnetic stability in dysprosium single atom magnets, Nano Lett. **21**, 8266 (2021).

[11] A. Singha, P. Willke, T. Bilgeri, X. Zhang, H. Brune, F. Donati, A. J. Heinrich, and T. Choi, Engineering atomic-scale magnetic fields by dysprosium single atom magnets, Nat. Commun. **12**, 4179 (2021).

[12] V. Bellini et al., Slow magnetic relaxation of Dy adatoms with in-plane magnetic anisotropy on a two-dimensional electron gas, ACS Nano **16**, 11182 (2022).

[13] S. Bertaina, S. Gambarelli, A. Tkachuk, I. N. Kurkins, B. Malkin, A. Stepanov, and B. Barbara, Rare-earth solid-state qubits, Nat. Nanotechnol. **2**, 39 (2007).

[14] S. Loth, K. von Bergmann, M. Ternes, A. Otte, C. Lutz, and A. Heinrich, Controlling the state of quantum spins with electric currents, Nat. Phys. **6**, 340 (2010).

[15] A. A. Khajetoorians, J. Wiebe, B. Chilian, and R. Wiesendanger, Realizing all-spin–based logic operations atom by atom, Science **332**, 1062 (2011).

[16] R. Vincent, S. Klyatskaya, M. Ruben, W. Wernsdorfer, and F. Balestro, Electronic read-out of a single nuclear spin using a molecular spin transistor, Nature (London) **488**, 357360 (2012).

[17] A. Khajetoorians, B. Baxevanis, C. Hübner, T. Schlenk, S. Krause, T. Wehling, S. Lounis, A. Lichtenstein, D. Pfannkuche, J. Wiebe, and R. Wiesendanger, Current-driven spin dynamics of artificially constructed quantum magnets, Science **339**, 55 (2013).

[18] S. Thiele, F. Balestro, R. Ballou, S. Klyatskaya, M. Ruben, and W. Wernsdorfer, Electrically driven nuclear spin resonance in single-molecule magnets, Science **344**, 1135 (2014).

[19] S. Baumann, W. Paul, T. Choi, C. P. Lutz, A. Ardavan, and A. J. Heinrich, Electron paramagnetic resonance of individual atoms on a surface, Science **350**, 417 (2015).

[20] C. Godfrin, A. Ferhat, R. Ballou, S. Klyatskaya, M. Ruben, W. Wernsdorfer, and F. Balestro, Operating Quantum States in Single Magnetic Molecules: Implementation of Grover's Quantum Algorithm, Phys. Rev. Lett. **119**, 187702 (2017).

[21] W. Paul, K. Yang, S. Baumann, N. Romming, T. Choi, C. P. Lutz, and A. J. Heinrich, Control of the millisecond spin lifetime of an electrically probed atom, Nat. Phys. **13**, 403 (2017).

[22] B. Kiraly, A. N. Rudenko, W. M. J. van Weerdenburg, D. Wegner, M. I. Katsnelson, and A. A. Khajetoorians, An orbitally derived single-atom magnetic memory, Nat. Commun. **9**, 3904 (2018).

[23] K. Yang, W. Paul, S.-H. Phark, P. Willke, Y. Bae, T. Choi, T. Esat, A. Ardavan, A. J. Heinrich, and C. P. Lutz, Coherent spin manipulation of individual atoms on a surface, Science **366**, 509 (2019).

[24] B. Verlhac, N. Bachellier, L. Garnier, M. Ormaza, P. Abufager, R. Robles, M.-L. Bocquet, M. Ternes, N. Lorente, and L. Limot, Atomic-scale spin sensing with a single molecule at the apex of a scanning tunneling microscope, Science **366**, 623 (2019).

[25] L. Malavolti, G. McMurtrie, S. Rolf-Pissarczyk, S. Yan, J. A. J. Burgess, and S. Loth, Minimally invasive spin sensing with scanning tunneling microscopy, Nanoscale **12**, 11619 (2020).

[26] H. Biard, E. Moreno-Pineda, M. Ruben, E. Bonet, W. Wernsdorfer, and F. Balestro, Increasing the Hilbert space dimension using a single coupled molecular spin, Nat. Commun. **12**, 4443 (2021).

[27] L. M. Veldman, L. Farinacci, R. Rejali, R. Broekhoven, J. Gobeil, D. Coffey, M. Ternes, and A. F. Otte, Free coherent evolution of a coupled atomic spin system initialized by electron scattering, Science **372**, 964968 (2021).

[28] X. Zhang, C. Wolf, Y. Wang, H. Aubin, T. Bilgeri, P. Willke, A. J. Heinrich, and T. Choi, Electron spin resonance of single iron phthalocyanine molecules and role of their non-localized spins in magnetic interactions, Nat. Chem. **14**, 5965 (2022).

[29] V. Dubrovin, A. A. Popov, and S. Avdoshenko, Magnetism in Ln molecular systems with $4f$/valence-shell interplay (FV-magnetism), Chem. Commun. **55**, 13963 (2019).

[30] V. Dubrovin, A. A. Popov, and S. M. Avdoshenko, Valence electrons in lanthanide-based single-atom magnets: A paradigm shift in 4f-magnetism modeling and design, Inorg. Chem. Front. **8**, 2373 (2021).

[31] F. Liu, D. S. Krylov, L. Spree, S. M. Avdoshenko, N. A. Samoylova, M. Rosenkranz, A. Kostanyan, T. Greber, A. U. B. Wolter, B. Büchner, and A. A. Popov, Single molecule magnet with an unpaired electron trapped between two lanthanide ions inside a fullerene, Nat. Commun. **8**, 16098 (2017).

[32] C. A. Gould, K. R. McClain, D. Reta, J. G. C. Kragskow, D. A. Marchiori, E. Lachman, E.-S. Choi, J. G. Analytis, R. D. Britt, N. F. Chilton, B. G. Harvey, and J. R. Long, Ultrahard magnetism from mixed-valence dilanthanide complexes with metal-metal bonding, Science **375**, 198 (2022).

[33] M. Pivetta, F. Patthey, I. Di Marco, A. Subramanian, O. Eriksson, S. Rusponi, and H. Brune, Measuring the Intra-Atomic Exchange Energy in Rare-Earth Adatoms, Phys. Rev. X **10**, 031054 (2020).

[34] M. Pivetta, S. Rusponi, and H. Brune, Direct capture and electrostatic repulsion in the self-assembly of rare-earth atom superlattices on graphene, Phys. Rev. B **98**, 115417 (2018).

[35] See Supplemental Material at http://link.aps.org/supplemental/10.1103/PhysRevLett.130.106702 for additional information on experimental and model details, and on the specific role of the individual fit parameters, which includes Refs. [36–63].

[36] R. Gaisch, J. K. Gimzewski, B. Reihl, R. R. Schlittler, M. Tschudy, and W. D. Schneider, Low-temperature ultra-high

[37] P. Forrester, T. Bilgeri, F. Patthey, H. Brune, and F. D. Natterer, Antiferromagnetic MnNi tips for spin-polarized scanning probe microscopy, Rev. Sci. Instrum. **89**, 123706 (2018).

[38] P.-G. de Gennes, Sur les propriétés des métaux des terres rares, C.R. Acad. Sci. **247**, 1836 (1958).

[39] P.-G. de Gennes, Interactions indirectes entre couches $4f$ dans les métaux de terres rares, J. Phys. Radium **23**, 510 (1962).

[40] L. L. Hirst, Theory of the coupling between conduction electrons and moments of $3d$ and $4f$ ions in metals, Adv. Phys. **27**, 231 (1978).

[41] S. Blundell, *Magnetism in Condensed Matter* (Oxford University Press, New York, 2001).

[42] R. Skomski, *Simple Models of Magnetism* (Oxford University Press, New York, 1996).

[43] R. Ahuja, S. Auluck, B. Johansson, and M. S. S. Brooks, Electronic structure, magnetism, and Fermi surfaces of Gd and Tb, Phys. Rev. B **50**, 5147 (1994).

[44] R. Baltic, F. Donati, A. Singha, C. Wäckerlin, J. Dreiser, B. Delley, M. Pivetta, S. Rusponi, and H. Brune, Magnetic properties of single rare-earth atoms on graphene/Ir(111), Phys. Rev. B **98**, 024412 (2018).

[45] K. Stevens, Matrix elements and operator equivalents connected with the magnetic properties of rare earth ions, Proc. Phys. Soc. London Sect. A **65**, 209 (1952).

[46] P. Politi, A. Rettori, F. Hartmann-Boutron, and J. Villain, Tunneling in Mesoscopic Magnetic Molecules, Phys. Rev. Lett. **75**, 537 (1995).

[47] C. Cervetti, A. Rettori, M. Pini, A. Cornia, A. Repollés, F. Luis, M. Dressel, S. Rauschenbach, K. Kern, M. Burghard, and L. Bogani, The classical and quantum dynamics of molecular spins on graphene, Nat. Mater. **15**, 164 (2016).

[48] E. Callen and H. B. Callen, Magnetostriction, forced magnetostriction, and anomalous thermal expansion in ferromagnets, Phys. Rev. **139**, A455 (1965).

[49] D. Coffey, J. L. Diez-Ferrer, D. Serrate, M. Ciria, C. de la Fuente, and J. I. Arnaudas, Antiferromagnetic spin coupling between rare earth adatoms and iron islands probed by spin-polarized tunneling, Sci. Rep. **5**, 13709 (2015).

[50] P. Anderson, Localized Magnetic States and Fermi-Surface Anomalies in Tunneling, Phys. Rev. Lett. **17**, 95 (1966).

[51] J. Schrieffer and P. Wolff, Relation between the Anderson and Kondo Hamiltonians, Phys. Rev. **149**, 491 (1966).

[52] J. Appelbaum, Exchange model of zero-bias tunneling anomalies, Phys. Rev. **154**, 633 (1967).

[53] M. Ternes, Spin excitations and correlations in scanning tunneling spectroscopy, New J. Phys. **17**, 063016 (2015).

[54] M. N. Leuenberger and D. Loss, Spin tunneling and phonon-assisted relaxation in Mn_{12}-acetate, Phys. Rev. B **61**, 1286 (2000).

[55] D. Gatteschi, R. Sessoli, and J. Villain, *Molecular Nanomagnets* (Oxford University Press, New York, 2006).

[56] A. Abragam, *The Principles of Nuclear Magnetism* (Clarendon Press, Oxford, 1961).

vacuum scanning tunneling microscope, Ultramicroscopy **42–44**, 1621 (1992).

[57] J. Villain, A. Würger, A. Fort, and A. Rettori, Effet tunnel dans les systèmes magnétiques: de la description microscopique et déterministe à l'équation maîtresse, J. Phys. I (France) **7**, 1583 (1997).

[58] F. Luis, J. Bartolomé, and J. F. Fernández, Resonant magnetic quantum tunneling through thermally activated states, Phys. Rev. B **57**, 505 (1998).

[59] L. Falkovsky, Phonon dispersion in graphene, J. Exp. Theor. Phys. **105**, 397 (2007).

[60] F. D. Natterer, F. Patthey, T. Bilgeri, P. Forrester, N. Weiss, and H. Brune, Upgrade of a low-temperature scanning tunneling microscope for electron-spin resonance, Rev. Sci. Instrum. **90**, 013706 (2019).

[61] A. A. Sapozhnik, C. Luo, H. Ryll, F. Radu, M. Jourdan, H. Zabel, and H. J. Elmers, Experimental determination of exchange constants in antiferromagnetic Mn_2Au, Phys. Rev. B **97**, 184416 (2018).

[62] S. Picozzi and A. Freeman, Polarization reduction in half-metallic Heusler alloys: The effect of point defects and interfaces with semiconductors, J. Phys. Condens. Matter **19**, 315215 (2007).

[63] F. Delgado, J. J. Palacios, and J. Fernández-Rossier, Spin-Transfer Torque on a Single Magnetic Adatom, Phys. Rev. Lett. **104**, 026601 (2010).

[64] A. Fort, A. Rettori, J. Villain, D. Gatteschi, and R. Sessoli, Mixed Quantum-Thermal Relaxation in Mn_{12} Acetate Molecules, Phys. Rev. Lett. **80**, 612 (1998).

[65] F. Delgado and J. Fernández-Rossier, Spin dynamics of current-driven single magnetic adatoms and molecules, Phys. Rev. B **82**, 134414 (2010).

[66] These measurements are characterized by an invariant phonon contribution. Hence, the bias voltage is the only parameter determining the spin reversal path. Identical fit parameters are used for both, temperature and bias dependent experiments, further confirming that spin-phonon scattering is negligible also in the Arrhenius plot.

[67] G. E. Pacchioni, L. Gragnaniello, F. Donati, M. Pivetta, G. Autès, O. V. Yazyev, S. Rusponi, and H. Brune, Multiplet features and magnetic properties of Fe on Cu(111): From single atoms to small clusters, Phys. Rev. B **91**, 235426 (2015).

[68] S. G. McAdams, A.-M. Ariciu, A. K. Kostopoulos, J. P. Walsh, and F. Tuna, Molecular single-ion magnets based on lanthanides and actinides: Design considerations and new advances in the context of quantum technologies, Coord. Chem. Rev. **346**, 216 (2017).

[69] N. Ishikawa, M. Sugita, N. Tanaka, T. Ishikawa, S.-y. Koshihara, and Y. Kaizu, Upward temperature shift of the intrinsic phase lag of the magnetization of bis(phthalocyaninato)terbium by ligand oxidation creating an $S = 1/2$ spin, Inorg. Chem. **43**, 5498 (2004).

[70] M. Urdampilleta, S. Klyatskaya, M. Ruben, and W. Wernsdorfer, Magnetic interaction between a radical spin and a single-molecule magnet in a molecular spin-valve, ACS Nano **9**, 4458 (2015).

[71] S. Demir, I.-R. Jeon, J. R. Long, and T. D. Harris, Radical ligand-containing single-molecule magnets, Coord. Chem. Rev. **289–290**, 149 (2015).

[72] D. Komijani, A. Ghirri, C. Bonizzoni, S. Klyatskaya, E. Moreno-Pineda, M. Ruben, A. Soncini, M. Affronte, and S. Hill, Radical-lanthanide ferromagnetic interaction in a Tb^{III} bis-phthalocyaninato complex, Phys. Rev. Mater. **2**, 024405 (2018).

[73] R. Pederson, A. L. Wysocki, N. Mayhall, and K. Park, Multireference *ab initio* studies of magnetic properties of terbium-based single-molecule magnets, J. Phys. Chem. A **123**, 6996 (2019).

[74] T. Frauhammer, H. Chen, T. Balashov, G. Derenbach, S. Klyatskaya, E. Moreno-Pineda, M. Ruben, and W. Wulfhekel, Indirect Spin-Readout of Rare-Earth-Based Single-Molecule Magnet with Scanning Tunneling Microscopy, Phys. Rev. Lett. **127**, 123201 (2021).

[75] J. D. Rinehart, M. Fang, W. J. Evans, and J. R. Long, A N_2^{3-} radical-bridged terbium complex exhibiting magnetic hysteresis at 14 K, J. Am. Chem. Soc. **133**, 14236 (2011).

[76] S. Demir, M. I. Gonzalez, L. Darago, W. J. Evans, and J. R. Long, Giant coercivity and high magnetic blocking temperatures for N_2^{3-} radical-bridged dilanthanide complexes upon ligand dissociation, Nat. Commun. **8**, 2144 (2017).